

Article

α -Manganese Dioxide (α -MnO₂) Coated with Polyaniline (PANI) and Reduced Graphene Oxide (rGO)-Based Nanocomposite for Supercapacitor Application

Pranoti H. Patil¹, Vidya V. Kulkarni¹, Tukaram D. Dongale² and Sushilkumar A. Jadhav^{1,*} ¹ School of Nanoscience and Technology, Shivaji University Kolhapur, Vidyanagar, Kolhapur 416004, India² Computational Electronics and Nanoscience Research Laboratory, School of Nanoscience and Technology, Shivaji University, Kolhapur 416004, India

* Correspondence: sushil.unige@gmail.com; Tel.: +91-0231-260-9000

Abstract: This work reports the preparation and testing of a composite material composed of α -Manganese dioxide (α -MnO₂) coated with polyaniline (PANI) and reduced graphene oxide (rGO) for supercapacitor application. The structure and morphology of the materials were characterized by using X-ray diffraction (XRD) analysis, Fourier transform infrared spectroscopy (FTIR), transmission electron microscopy (TEM), thermogravimetric analysis (TGA) and Raman spectroscopy. The electrochemical performances of the materials were investigated by using cyclic voltammetry (CV), Galvanostatic charge–discharge (GCD), cyclic stability and electrochemical impedance spectroscopy (EIS). The α -MnO₂-coated PANI/rGO nanocomposite exhibited a specific capacitance of 261 F g⁻¹ at the scan rate of 5 mV s⁻¹ with 75% capacitance retention after 2000 cycles at 5 A g⁻¹. It showed a specific energy of 11 W h kg⁻¹ and specific power of 1250 W kg⁻¹.

Keywords: polyaniline; manganese dioxide; reduced graphene oxide; specific capacitance; supercapacitor



Citation: Patil, P.H.; Kulkarni, V.V.; Dongale, T.D.; Jadhav, S.A.

α -Manganese Dioxide (α -MnO₂) Coated with Polyaniline (PANI) and Reduced Graphene Oxide (rGO)-Based Nanocomposite for Supercapacitor Application. *J. Compos. Sci.* **2023**, *7*, 167. <https://doi.org/10.3390/jcs7040167>

Academic Editor: Francesco Tornabene

Received: 5 March 2023

Revised: 3 April 2023

Accepted: 13 April 2023

Published: 16 April 2023



Copyright: © 2023 by the authors. Licensee MDPI, Basel, Switzerland. This article is an open access article distributed under the terms and conditions of the Creative Commons Attribution (CC BY) license (<https://creativecommons.org/licenses/by/4.0/>).

1. Introduction

Energy storage systems such as batteries, fuel cells, electrochemical capacitors and solar cells are currently the subject of intense research. Every portable electronic device demands high power density over long periods of time. Due to their electrochemical performance in comparison to other energy storage devices, supercapacitors (SCs) have demonstrated that they are capable of doing so [1,2]. Despite having high power density, SCs are unable to meet the high energy density requirements, particularly for use in electric vehicles. There is a need to develop a hybrid SC in order to address the poor energy density [3]. According to the charge storage mechanism, SCs are classified into three types, pseudocapacitors, electric double layer capacitors (EDLCs) and hybrid SCs [4]. Graphene is a potential electrode material for SC applications. It is difficult to process and is extensively surface functionalized to enhance processability [5]. On the other hand, hybrid SCs overcome the limits of EDLCs and pseudocapacitors. The capacitance of a redox capacitor is provided by faradic or pseudo-redox processes that occur within the active materials of the electrode [6–8]. Conducting polymers (CPs) such as polyaniline (PANI) are preferred as electrode materials for SCs due to their high specific capacitance and superior electrical conductivity. However, their weak cyclic stability limit their practical application [9]. Manganese dioxide (MnO₂) is a transition metal oxide (TMO) that has been widely employed as an electrode material for SCs due to its outstanding theoretical capacitance (1370 F g⁻¹), low cost and availability [10]. However, its low conductivity restricts its potential applications. As a result, composite materials composed of MnO₂ and CPs have gained importance for SC applications. It has been demonstrated that composites may fully take advantage of both MO and CP components. The shape and interfacial

properties of the mixture as well as the specific materials used influence the properties of nanocomposite-based electrodes. The flexibility, toughness and coatability of polymers as well as the hardness and durability of MOs are all advantages of CP/MO nanocomposites [11]. Binary composite materials generally include CP/MO composites. Ternary composites have gained the attention of many researchers because of their tremendous advantages in improving the overall performance of materials. Carbonaceous materials such as graphene, reduced graphene oxide (rGO) and carbon nanotubes (CNTs) will boost the capacitance values of materials. Graphene or graphene oxide (GO) is considered to be a good scaffold, especially compared to carbon nanotubes, due to its high surface area, outstanding mechanical and electrical properties as well as good conductivity [12]. For instance, in an experiment performed by Ates and Yildirim, they chemically synthesized RuO₂/PANI and rGO/RuO₂/PANI nanocomposites which yielded specific capacitance of 40.2 F g⁻¹ and 723.09 F g⁻¹, respectively [13]. Liu et al. synthesized ternary hierarchical nanofiber MnO₂/PANI/MWCNT, and it exhibited the highest capacitance of 348.5 F g⁻¹ at 1 A g⁻¹, and 88.2% capacitance was maintained after 2000 consecutive cycles [14]. Hou et al. synthesized a MnO₂ nanosphere/CNT/CP ternary composite that exhibited specific capacitance of 427 F g⁻¹. The composite displayed good cycling stability of 99% capacitance retention [15]. Yu et al. prepared graphene/MnO₂/CP composites, and compared with CNTs and CPs, the capacitance of the electrodes was substantially increased by ~20% and ~45%, respectively. Moreover, these ternary composite electrodes have also exhibited excellent cycling performance with >95% capacitance retention over 3000 cycles [16]. Vignesh et al. synthesized an R7//Ni-Co-Zn-S electrode material for an asymmetric supercapacitor which exhibited high energy density of 53.1 W h kg⁻¹ with the power density of 800 W kg⁻¹ at a current density of 1 A g⁻¹ [17]. Vignesh et al. synthesized a graphene nanosheet (GNS)-supported manganese sulfide (MnS) hybrid nanocomposite via the facile hydrothermal process. The nanocomposite exhibited high capacitance of 792 F g⁻¹ at a current density of 2 A g⁻¹ with 91.1% capacitance retention after 15,000 cycles. The hybrid electrode material also showed energy density of 25 W h kg⁻¹ and also delivered high power density of 7160 W kg⁻¹ [18].

These representative examples discussed above highlight the importance of MO-CP and carbonaceous-material-based composites for SC application. This is why, recently, such hybrid composites are being studied for supercapacitor applications. The electrochemical properties of each component of such composites helps to tune the overall performance, such as the capacitance, energy and power density of the device. In this work, we have successfully synthesized a ternary nanocomposite named α -MnO₂/PANI/rGO. The metal oxide was coated with CP via an in situ oxidative polymerization process to overcome the drawbacks of improper polymer distribution in the composite. The final composite was obtained by adding rGO to α -MnO₂/PANI material. The comparison of the electrochemical performance of individual components and binary and ternary nanocomposites demonstrates that rGO has a synergistic impact on the response of the material.

2. Experimental Section

2.1. Materials

MnSO₄·H₂O (99%) was purchased from SD Fine chem. Ltd., and KMnO₄ (99%), H₂SO₄ (98%) and H₂O₂ (30% w/v) were acquired from Thomas Baker. Chemicals such as, aniline, ammonium per sulfate (APS), N-methylpyrrolidone (NMP, 99%) and conc. HCl (98%) were obtained from Sigma Aldrich. Ethanol was purchased from Changshu Hongsheng Fine Chemicals Co., Ltd. (Changshu, China).

2.2. Instruments and Methods

The X-ray diffraction (XRD) patterns were registered on a Bruker AXS D8 Advance diffractometer with copper source used as a target for X-ray production (CuK α , λ = 1.5405Å), with 2 θ ranging from 0° to 80°. The transmission electron microscopy (TEM) images were taken with a JEOL 2011 instrument operated at 300 kV and equipped with a LaB6

filament. The surface morphologies of the prepared samples were investigated via field emission scanning electron microscopy (FE-SEM, JEOL JSM 6390). The Fourier transform infrared (FTIR) spectra were recorded with a Bruker ALPHA spectrometer. Thermogravimetric analyses (TGAs) were carried out on an SDT Q600 V20.9 Build 20 with TA Instruments by heating samples in nitrogen atmosphere from room temperature to 900 °C with 10 °C min⁻¹. Raman shift was registered on a Renishaw INCIA0120-20 from 500 to 3000 cm⁻¹ wavelength.

2.3. Synthesis

2.3.1. Synthesis of α -MnO₂

The reaction mixture was prepared by adding 100 mL of 0.1 M KMnO₄ solution to a 100 mL 0.15 M MnSO₄·4H₂O solution. Later, it was kept under vigorous stirring on a magnetic stirrer for 5 h at room temperature until dark brown precipitate was obtained at the bottom of a round-bottom flask (RBF). The obtained product was centrifuged and washed 2–3 times with distilled water followed by being dried in a hot air oven at 70 °C overnight.

2.3.2. Synthesis of PANI

PANI was synthesized by the oxidative polymerization of aniline. For this, 14.24 g of APS was dissolved in 25.5 mL of distilled water using a magnetic stirrer for 5 min. Then, 4.6 mL aniline was added to 50 mL of 1 M HCl. The aniline solution was transferred to RBF and kept under stirring in ice-cold conditions. The reaction mixture was kept under vigorous stirring for 6–8 h. Later, the product was centrifuged, washed with water and ethanol and dried overnight at 80 °C.

2.3.3. Synthesis of PANI-Coated α -MnO₂

The synthesized α -MnO₂ powder was suspended in 200 mL of 0.5 M H₂SO₄, and 1.8 mL of aniline was added to it. Then, the dropwise addition of 0.3 M FeCl₃ (200 mL) was carried out at about 0 °C. The greenish-black precipitate of the α -MnO₂/PANI nanocomposite obtained was centrifuged and washed several times with distilled water and ethanol for the elimination of low-molecular-weight polymers. The product was dried at 70 °C.

2.3.4. rGO Synthesis

GO powder (500 mg) was sonicated in milliQ water (60 mL) for 20 min. Hydrazine hydrate (15 mL) was added to the dispersed suspension. After that, the mixture was refluxed at 98 °C for 24 h. The product was recovered by centrifugation and washed with diluted HCl and then washed several times with water. It was finally dried in an oven.

2.4. Electrode Fabrication

Stainless steel substrates (5 cm × 1 cm) were etched using an etchant solution prepared by mixing conc. HCl (8 mL) diluted up to 10 mL, and H₂O₂ (10 mL) was added to it (1:1 ratio). The substrates were dipped in this etchant solution for 1 ½ h and cleaned using ethanol. The working electrodes were prepared by mixing active material, polyvinylidene fluoride (PVDF) and carbon black in the ratio of 8:1:1 using NMP as a solvent. The thin film of the material was pasted on etched substrates in a 1 cm² area using the Doctor Blade method. The prepared electrodes were dried at 90 °C for 12 h. The weight of electrodes before and after coating was noted to calculate the mass loading.

3. Results and Discussion

3.1. Characterizations

3.1.1. XRD

XRD was used to analyze the structural properties of the synthesized MnO₂ particles. As shown in Figure 1A, sharp diffraction peaks were observed in the XRD of MnO₂ at 2 θ of 12.79°, 17.99°, 28.7°, 37.38°, 42.02°, 58.18°, 60.18° and 65.46°, which are well indexed to the (110), (200), (310), (211), (301), (411), (521) and (002) crystal planes of

tetragonal MnO_2 , respectively. These diffraction peaks are attributed to the $\alpha\text{-MnO}_2$ crystal phase, and the data agree well with the JSPDS 44-0141 card [19,20], indicating that tetragonal crystalline MnO_2 was successfully synthesized. The XRD pattern of the $\alpha\text{-MnO}_2/\text{PANI}/\text{rGO}$ nanocomposite is shown in Figure 1A, and it showed additional peaks at 23° and 27° , which indicated the presence of PANI (113) and rGO (310) in the composite. All other sharp peaks were assigned to the $\alpha\text{-MnO}_2$. This information revealed that the nanocomposite was successfully synthesized [21,22]. The average crystallite size of the particles was determined using the Debye Scherer equation $D_p = (K k) / (b \cdot \cos \theta)$, where 'K' is the form factor. 'k' represents the X-ray wavelength, 'b' represents the XRD peak's full wave half maximum (FWHM), and 'h' represents the Bragg's angle. The average crystallite size was 15 nm.

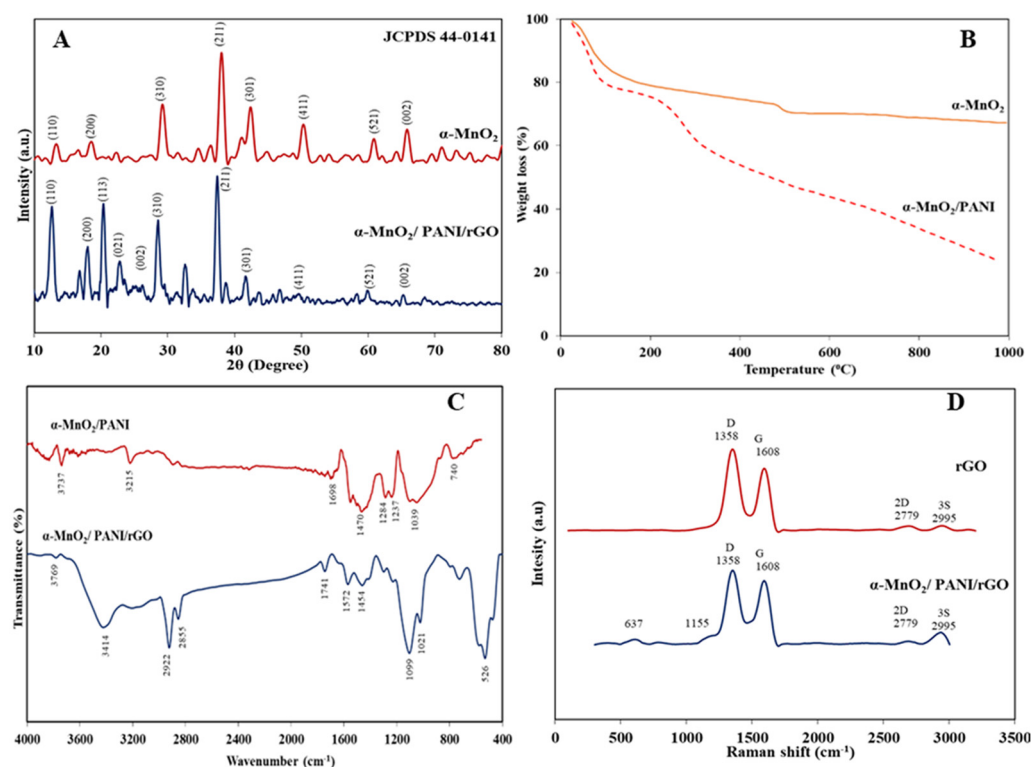


Figure 1. (A) XRD patterns of $\alpha\text{-MnO}_2$ and $\alpha\text{-MnO}_2/\text{PANI}/\text{rGO}$, (B) TGA curves of MnO_2 and $\text{MnO}_2\text{-PANI}$ samples, (C) FTIR spectra of $\alpha\text{-MnO}_2\text{-PANI}$ and $\alpha\text{-MnO}_2/\text{PANI}/\text{rGO}$, (D) Raman spectra of rGO and $\alpha\text{-MnO}_2/\text{PANI}/\text{rGO}$ sample.

3.1.2. TGA

TGA was used to quantify the amount of the polymer coated on MnO_2 . Figure 1B depicts the TGA curves of $\alpha\text{-MnO}_2$ and $\alpha\text{-MnO}_2/\text{PANI}$. The weight loss of the bare $\alpha\text{-MnO}_2$ sample was approximately 16% up to 100°C due to residual water evaporation and 16% between 100°C and 1000°C [23]. As a result, the overall weight loss of $\alpha\text{-MnO}_2$ was roughly 32%. However, up to 100°C , the $\alpha\text{-MnO}_2/\text{PANI}$ nanocomposite showed 20% weight loss and 18% weight loss between 100 and 300°C . Weight loss of 34% was recorded from 300°C to 1000°C , resulting in a total weight loss of 72% for $\alpha\text{-MnO}_2/\text{PANI}$. As a result, the amount of the PANI coated on MnO_2 was 39% PANI.

3.1.3. IR

The FTIR spectrum was used to analyze the intermolecular interactions and vibrational properties of the compounds. Figure 1C depicts the IR spectrum of the $\alpha\text{-MnO}_2\text{-PANI}$ and $\alpha\text{-MnO}_2\text{-PANI}/\text{rGO}$ nanocomposites. The $\alpha\text{-MnO}_2\text{-PANI}$ nanocomposite revealed typical peaks ascribed to PANI and $\alpha\text{-MnO}_2$. In general, Mn-O bending vibrations have a characteristic peak in the 500 cm^{-1} to 900 cm^{-1} range [24]. The contribution of Mn-O

vibrations to the absorption band at 740 cm^{-1} verified the formation of $\alpha\text{-MnO}_2$, and the peaks at 1698 cm^{-1} and 1470 cm^{-1} were attributed to the C=C stretching vibration of the quinoid ring and the C=C stretching vibration of the benzenoid ring, respectively. The C-N stretching vibrations in the polymer chain were attributed to the bands at 1284 and 1237 cm^{-1} . The bands at 1039 cm^{-1} correspond to C-H stretching vibrations [25–27]. Because of the interaction between $\alpha\text{-MnO}_2$ and PANI, the N-H stretching vibration was observed as a broad (weak) curve near 3215 cm^{-1} , which may have resulted in charge transfer activity [28]. Two typical peaks observed at 1454 and 1572 cm^{-1} in the $\alpha\text{-MnO}_2/\text{PANI}/\text{rGO}$ composite were due to C=C stretching vibrations of the benzenoid and quinonoid rings, respectively. These distinctive peaks were consistent with the properties of the pure PANI, indicating that PANI was formed in the $\alpha\text{-MnO}_2/\text{PANI}/\text{rGO}$ composite. The peak observed at 3414 was attributed to OH stretching, while the peaks at 1741 and 1021 were assigned to C=O and C-O-C stretching, respectively, which confirmed the presence of rGO in $\alpha\text{-MnO}_2/\text{PANI}/\text{rGO}$ [29].

3.1.4. Raman Spectroscopy

Raman spectroscopy has been widely used to analyze material properties such as doping type, layer number as well as GO reduction processes. Raman spectra of rGO and $\alpha\text{-MnO}_2/\text{PANI}/\text{rGO}$ are shown in Figure 1D. The D- (1358 cm^{-1}), G- (1608 cm^{-1}), 2D- (2779 cm^{-1}) and 3S- (2995 cm^{-1}) peaks in Raman spectroscopy were representative of synthesized rGO, while the D peak represented the defect/disorder states of rGO, and the G peak was associated with the sp^2 bonding of carbon atoms [30]. The peaks at 1110 and 1512 cm^{-1} were related to the C-H bending and C=C stretching of the quinoid ring, respectively. The 1237 cm^{-1} peak was associated with the C-H bending of the benzenoid ring, and the peak at 1255 was related to C-N stretching vibrations [29,30].

3.1.5. TEM and FESEM

The TEM images of $\alpha\text{-MnO}_2/\text{PANI}$ are shown in Figure 2A,B. They showed mostly elongated rod shaped $\alpha\text{-MnO}_2$ material with aggregates in the polymeric mass with rough morphology for the oxide distributed in soft matter (polymer). The FESEM images of the composite are shown in Figure 2C,D. They mainly showed the presence of the polymer matrix aggregates as the underlying materials were coated with the polymer.

3.2. Electrochemical Testing

Electrochemical performance tests such as cyclic voltammetry (CV), Galvanostatic charge–discharge (GCD), electrochemical impedance spectroscopy (EIS) and cyclic stability were carried out using three-electrode assembly on an electrochemical workstation (biologic VSP3). The reference electrode and counter electrode were a Saturated Calomel Electrode (SCE) and a platinum wire, respectively. All the measurements were carried out in $0.5\text{ M H}_2\text{SO}_4$ as the electrolyte.

3.2.1. CV

CV is a potent and widely used electrochemical technique for studying the reduction and oxidation processes of materials, and it also gives insights into the relationships of structure, potential and characteristic activities. It is the technique that controls the voltage to measure the current which develops in an electrochemical cell. Figure 3A–D illustrate the CV curves of PANI, rGO, $\alpha\text{-MnO}_2/\text{PANI}$ and $\alpha\text{-MnO}_2/\text{PANI}/\text{rGO}$ nanocomposites at different scan rates ranging from 5 to 100 mV s^{-1} in a potential window of -0.2 V to 0.8 V for PANI and rGO and -0.3 V to 0.7 V for $\alpha\text{-MnO}_2/\text{PANI}$ and $\alpha\text{-MnO}_2/\text{PANI}/\text{rGO}$.

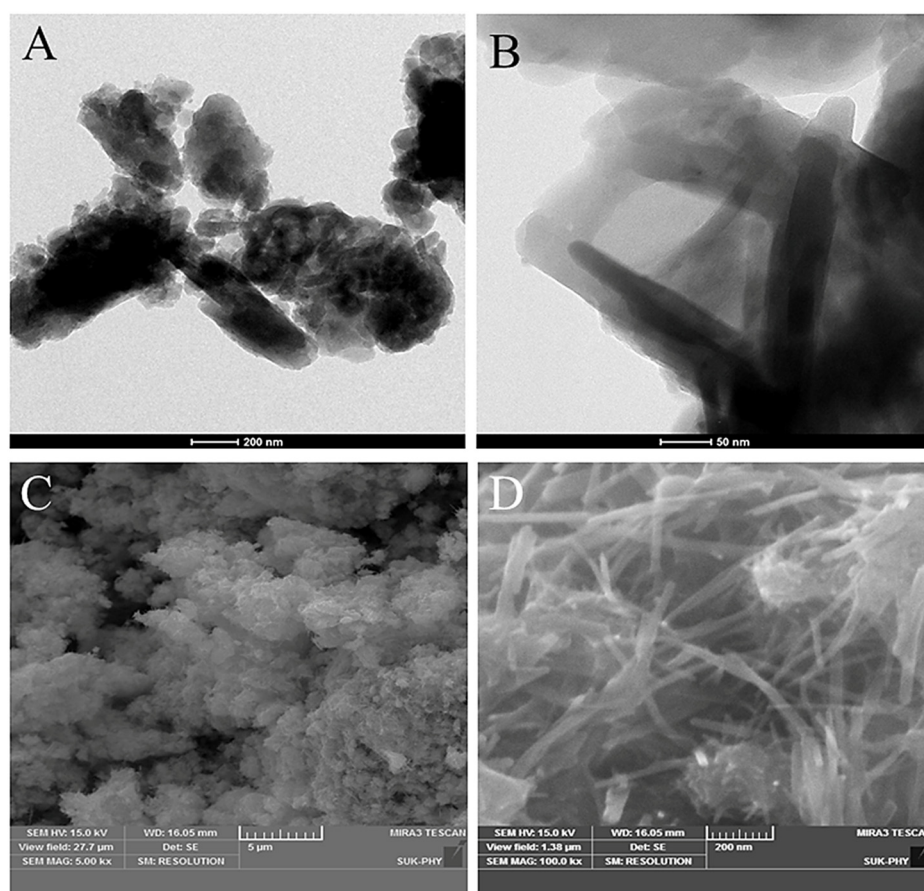


Figure 2. (A,B) TEM images of α -MnO₂-PANI composites at different magnifications. (C,D) FESEM images of the composites at different magnifications.

The shapes of all CV curves at the different scan rates exhibited redox peaks; peaks were observed at 0.3 V and 0.7 V in the oxidation process and at 0 V and 0.4 V in the reduction process, indicating the pseudocapacitive characteristics for PANI electrodes, which would produce CV curves of ideal rectangular shapes, and the internal resistance was responsible for the positive shift in the oxidation process and negative shift in the reduction process. From Figure 3A, it can be clearly seen that as the scan rate increased, the area under curve also increased, indicating electrochemical behavior. PANI existed in three states in this range, as shown in Figure 4.

The reduction peaks at (0 V and 0.4 V) and oxidation peaks (0.3 V and 0.7 V) of PANI were attributed to the redox conversion of leucoemeraldine to emeraldine (0.3 V and 0 V) and emeraldine to pernigraniline (0.7 V and 0.4 V), respectively [31]. It is clear that rGO as a supercapacitor electrode exhibited pseudocapacitive behavior rather than the typical electric double-layer capacitance with a rectangular CV shape. Figure 3B indicates that the oxygen functional groups in GO were not completely removed by the reduction process. The voltammograms of the synthesized α -MnO₂/PANI composite are shown in Figure 3C, in which nearly semi-rectangular shapes showed pseudocapacitive behavior and excellent reversibility in charging and discharging at a constant rate over the potential range of -0.3 V to 0.7 V. Figure 3D displays the CV curves of α -MnO₂/PANI/rGO at different scan rates in the voltage range -0.3 V to 0.7 V. It shows the pseudocapacitive behavior. It shows a semi-rectangular shape with large hump of redox couple observed at (0.25 V and -0.1 V). The largest capacitive current response and increase in the area of integration in the α -MnO₂/PANI/rGO nanocomposite was contributed to by the addition of rGO in the α -MnO₂/PANI composite. As the scan rate increased, the voltammograms show that the oxidation peaks moved toward the positive side, and reduction peaks moved toward the

negative side. During the oxidation–reduction processes, protons are exchanged with the electrolyte and electrode interface. Because this proton transfer process is slow, higher scan rates lead to either the depletion or saturation of the protons in the electrolyte inside the electrode during the redox process, which leads to the decrease in the capacitance values, whereas at a lower scan rate protons get sufficient time to interact with the electrode surface; that is, the full utilization of electrode material results in the highest capacitance value [31].

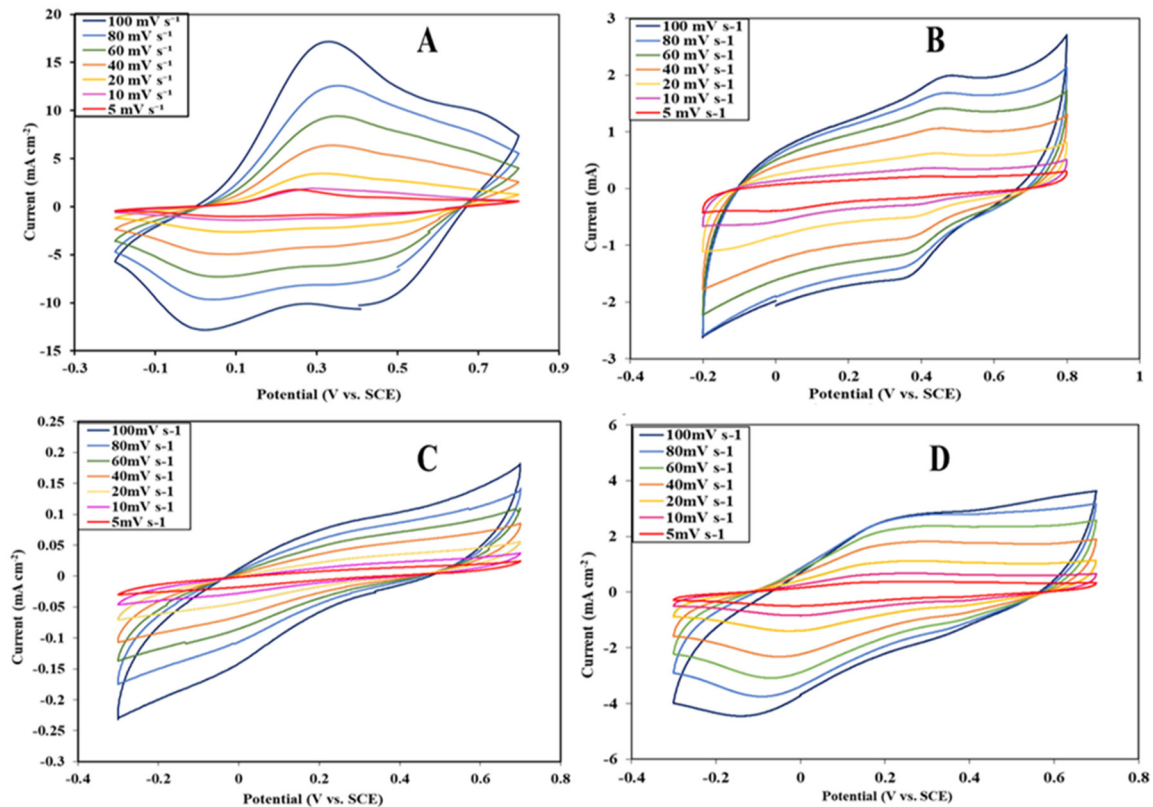


Figure 3. CV plots of (A) PANI, (B) rGO, (C) α-MnO₂/PANI and (D) α-MnO₂/PANI/rGO.

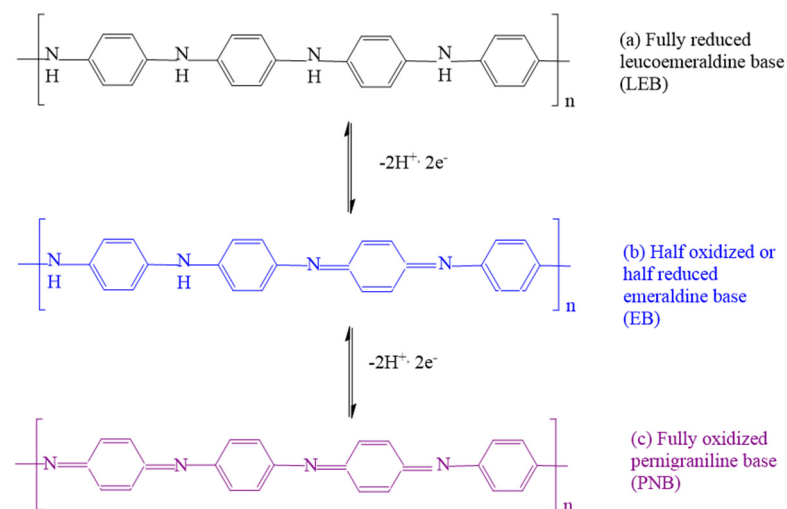


Figure 4. Schematic illustration for the electrochemical reaction mechanism of PANI.

The specific capacitance of each sample was calculated using the formula in Equation (1), where C_{sp} is the specific capacitance ($F g^{-1}$), m is the mass of working electrode

material (g), $(V_f - V_i)$ is the applied potential window (V), v is the scan rate (mVs^{-1}) and the integral term represents area under the CV curve [32].

$$C_{sp} = \frac{1}{m \times (V_f - V_i) \times v} \int_{V_i}^{V_f} I(V)dv \tag{1}$$

The specific capacitance values calculated from CV for the PANI, rGO, $\alpha\text{-MnO}_2/\text{PANI}$ composite and the $\alpha\text{-MnO}_2/\text{PANI}/\text{rGO}$ nanocomposite are represented in Table 1 and they are graphically shown in Figure 5. PANI showed the highest specific capacitance value of 604 F g^{-1} , and rGO showed the specific capacitance of 188 F g^{-1} at a scan rate of 5 mV s^{-1} . Furthermore, the $\alpha\text{-MnO}_2/\text{PANI}$ composite showed the capacitance of 13 F g^{-1} , while the $\alpha\text{-MnO}_2/\text{PANI}/\text{rGO}$ nanocomposite showed 261 F g^{-1} at the scan rate of 5 mV s^{-1} .

Table 1. Specific capacitance values calculated from CV.

Scan Rate (mVs^{-1})	Specific Capacitance (F g^{-1})			
	PANI	rGO	$\alpha\text{-MnO}_2/\text{PANI}$	$\alpha\text{-MnO}_2/\text{PANI}/\text{rGO}$
5	604	188	13	261
10	567	152	10	229
20	547	125	7	192
40	523	103	6	158
60	519	88	5	141
80	492	79	4	128
100	443	72	3	117

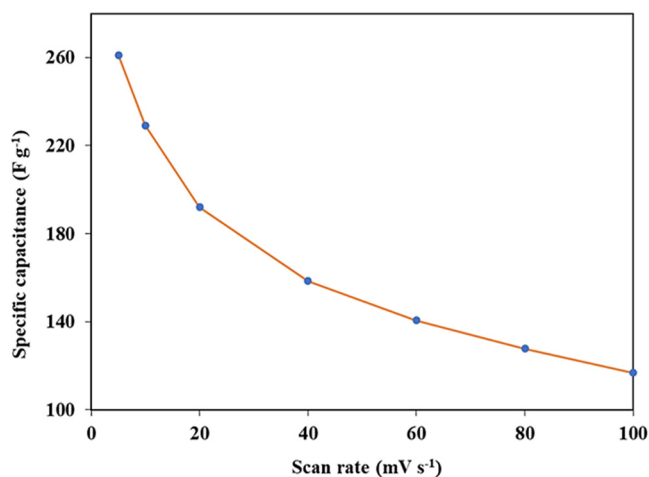


Figure 5. Plot of specific capacitance vs. scan rate of $\alpha\text{-MnO}_2/\text{PANI}/\text{rGO}$.

3.2.2. GCD

GCD is the technique where we fix the potential window and current to measure the time (charging and discharging time). Figure 6A,B show GCD cycles of PANI and rGO in the potential range of -0.2 V to 0.8 V , while Figure 6C,D show GCD cycles of $\alpha\text{-MnO}_2/\text{PANI}$ and $\alpha\text{-MnO}_2/\text{PANI}/\text{rGO}$ in the potential window -0.3 V to 0.7 V at different current densities such as 10 mA cm^{-2} , 8 mA cm^{-2} , 6 mA cm^{-2} , 4 mA cm^{-2} , 2 mA cm^{-2} and 1 mA cm^{-2} .

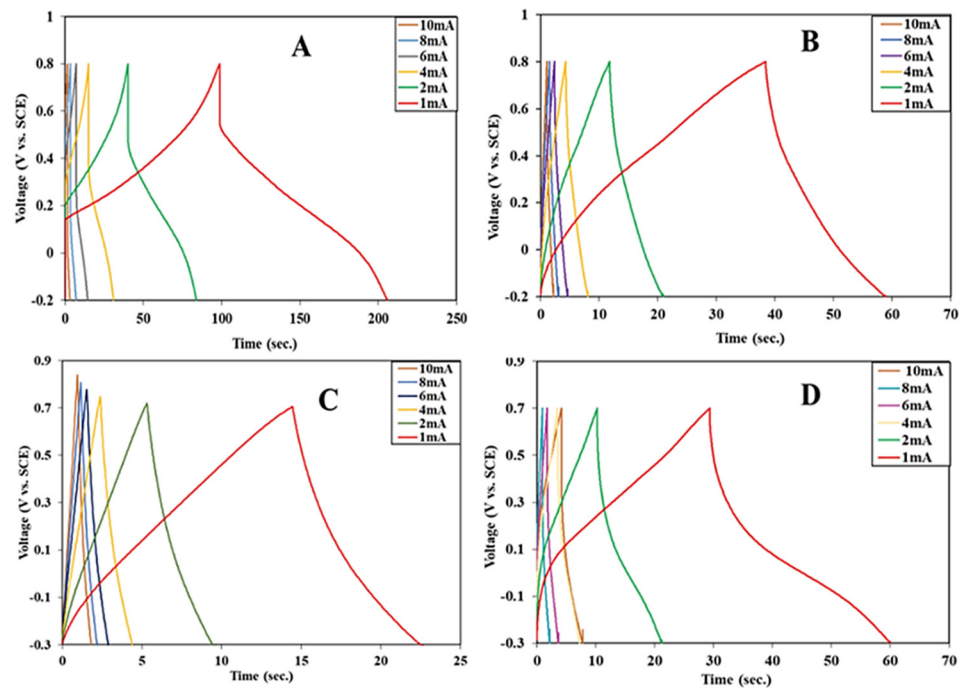


Figure 6. GCD cycles of (A) PANI, (B) rGO, (C) α -MnO₂/PANI and (D) α -MnO₂/PANI/rGO.

It can be seen that all the charge–discharge curves of PANI were not ideal straight lines, indicating the process of a faradic reaction and the capacitance arise from pseudocapacitance resulting from the fast reversible oxidation and reduction processes. The GCD cycles of PANI showed asymmetric triangular shapes, which represent pseudocapacitive behavior. A large amount of voltage drop (IR drop) could be seen at higher current densities, indicating high internal resistance. It can be noted that the curve exhibited asymmetric charge–discharge curves, indicating that the capacitance behavior of rGO was not the typical electric double-layer capacitance. A small amount of voltage drop (IR drop) was observed at higher current densities, which indicated small internal resistance. Furthermore, α -MnO₂/PANI and α -MnO₂/PANI/rGO exhibited asymmetric charge discharge curves in the potential window of -0.3 V to 0.7 V, which confirmed the pseudocapacitance properties of these electrode materials. No voltage drop (IR drop) was observed in the GCD cycles of α -MnO₂/PANI and α -MnO₂/PANI/rGO. It is evident that the α -MnO₂/PANI/rGO ternary nanocomposite delivered the highest specific capacitance compared to those of PANI, rGO and α -MnO₂/PANI.

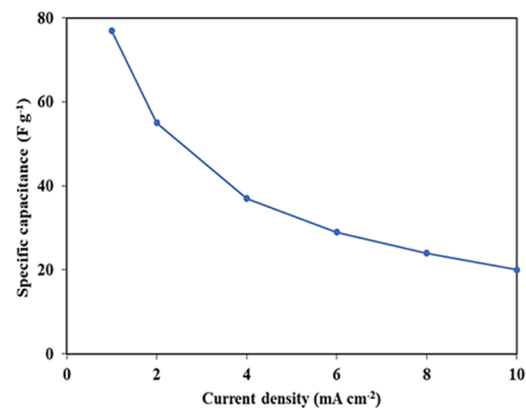
The specific capacitance was calculated by using the formula in Equation (2), where C_{sp} is the specific capacitance of the sample electrode, T_d is the discharge time, I_{dis} is the discharge current, m is the mass of the working electrode material, and $(V_f - V_i)$ is the applied potential window (V) [33].

$$C_{sp} = \frac{I_{dis} \times T_d}{(V_f - V_i) \times m} \quad (2)$$

The specific capacitance values obtained from GCD for the PANI, rGO, α -MnO₂/PANI and α -MnO₂/PANI/rGO nanocomposites are displayed in Table 2 and they are graphically shown in Figure 7. PANI showed the highest specific capacitance of 334 F g^{-1} , while rGO showed the specific capacitance of 51 F g^{-1} at a current density of 1 mA cm^{-2} . The α -MnO₂/PANI composite showed the specific capacitance of 13 F g^{-1} , while the α -MnO₂/PANI/rGO nanocomposite showed the specific capacitance of 77 F g^{-1} at 1 mA cm^{-2} .

Table 2. Specific capacitance values calculated from GCD.

Current Density (mA cm ⁻²)	Specific Capacitance (F g ⁻¹)			
	PANI	rGO	α-MnO ₂ /PANI	α-MnO ₂ /PANI/rGO
1	334	51	29	77
2	273	45	24	55
4	198	37	22	37
6	138	33	22	29
8	91	14	21	24
10	55	28	20	22

**Figure 7.** Plot of specific capacitance vs. current density of α-MnO₂/PANI/rGO.

Specific energy is the total amount of energy that can be stored in the device per unit of volume. However, the term specific power represents how fast a charged device can discharge. The specific energy and specific power were calculated using the following formulas from the given Equations (3) and (4):

$$E_{max} = \frac{0.5 \times C_{sp} \times V^2}{3.6} \quad (3)$$

$$P_{max} = \frac{3600 \times E_{max}}{\Delta t} \quad (4)$$

where C_{sp} is specific capacitance (F g⁻¹), E_{max} is the specific energy (W h kg⁻¹), P_{max} is the specific power (W kg⁻¹), V is the applied potential window (V), and Δt is the discharge time (s).

The specific energy values for PANI, rGO, α-MnO₂/PANI and α-MnO₂/PANI/rGO were 47 W h kg⁻¹, 7.0 W h kg⁻¹, 4.0 W h kg⁻¹ and 11 W h kg⁻¹, respectively, at corresponding power densities of 1563 W kg⁻¹, 1250 W kg⁻¹, 1250 W kg⁻¹ and 1250 W kg⁻¹. The Ragone plot of the α-MnO₂/PANI/rGO nanocomposite operating in the supercapacitor region is shown in Figure 8.

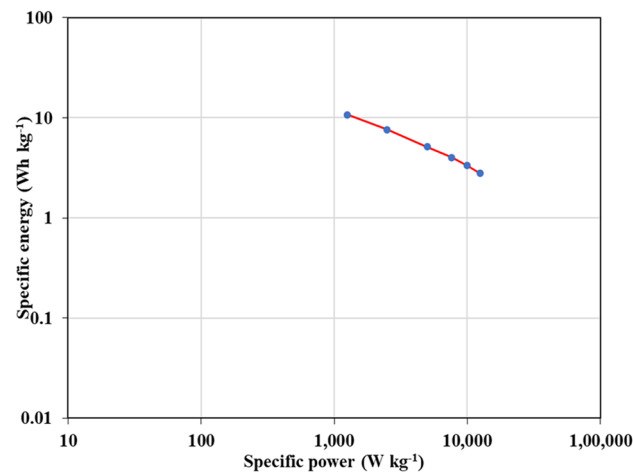


Figure 8. Ragone plot of α -MnO₂/PANI/rGO nanocomposite and all its components.

3.2.3. EIS

EIS analysis is an important technique to estimate the effects of conductivity, structure and charge transport in an electrode and electrolyte interface. EIS was performed over the frequency region of 200 kHz to 100 m Hz at an open circuit potential with 10 mV.

From the Nyquist plots (Figure 9), it is evident that pure PANI and α -MnO₂/PANI exhibited semicircles in the high-frequency region and linear spikes in the lower-frequency region. The initial nonzero intercept in the high-frequency region at Z' (real impedance) occurred at the beginning of the semicircle and was due to the electrical resistance of the electrolyte. Generally, contact resistance occurs between the electrolyte and current collector with active material. However, the plots of rGO and α -MnO₂/PANI/rGO did not exhibit semicircles in the high-frequency region due to the Faradic charge transfer resistances. The rGO, α -MnO₂/PANI and α -MnO₂/PANI/rGO electrodes displayed more vertical lines than PANI at low frequency, representing better the capacitive behavior and lower diffusion resistance of ions [34,35]. From the point intersection with the x-axis in the range of high frequency, the internal resistance could be evaluated. Internal resistance includes the ionic resistance of the electrolyte, the intrinsic resistance of the active material and the contact resistance at the interface of the active material and current collector [34]. Warburg resistance was indicated by a straight line, which was due to the diffusion of ions in the active electrode material in the low-frequency region [36]. All EIS except α -MnO₂/PANI showed distorted semicircles and vertical increasing linear spikes in the given frequency region. The amount of charge-transfer resistance could be determined using the semicircle's diameter. The least charge-transfer resistance was observed in rGO, while the maximum charge-transfer resistance was observed in PANI. Intermediate charge-transfer resistance was observed in α -MnO₂/PANI/rGO nanocomposite. The EIS of α -MnO₂/PANI showed a straight line. The measured EIS were analyzed via the equivalent circuit, which is shown in the inset of Figure 9. The average values obtained for R1 and R3 were 1.888 Ω and 1.079 Ω , respectively, while C2 and C3 displayed the values of 0.00002836 F and 0.01834 F, respectively.

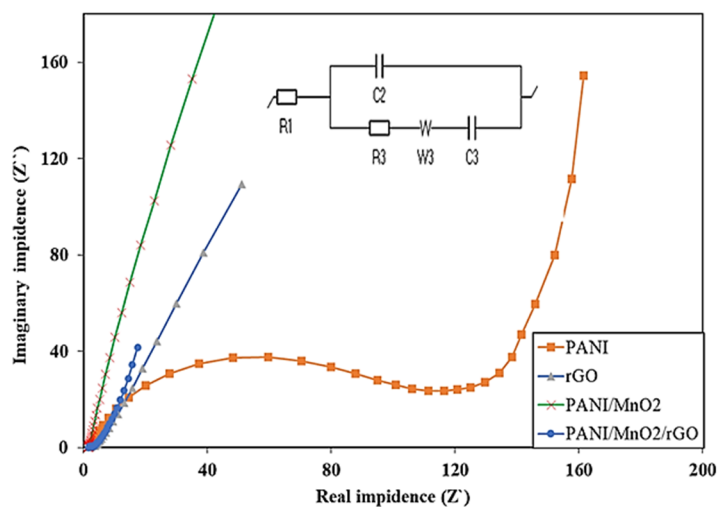


Figure 9. Nyquist plots of PANI, rGO, α -MnO₂/PANI and α -MnO₂/PANI/rGO.

3.2.4. Cyclic Stability

Long-term cycle stability is the most essential aspect for SC application. Therefore, the stability of the PANI, rGO and α -MnO₂/PANI/rGO electrodes were examined by conducting GCD measurements up to 2000 cycles in the potential range of -0.3 V to 0.7 V at a discharge current density of 5 mA cm^{-2} . Figure 10 illustrates the cyclic stability of the PANI, rGO and α -MnO₂/PANI/rGO nanocomposite, which displayed 57%, 71% and 75% capacitance retention after 2000 consecutive cycles, respectively. In the α -MnO₂/PANI/rGO nanocomposite, a very low linear drop of specific capacitance value was observed after 80%, which indicated good stability.

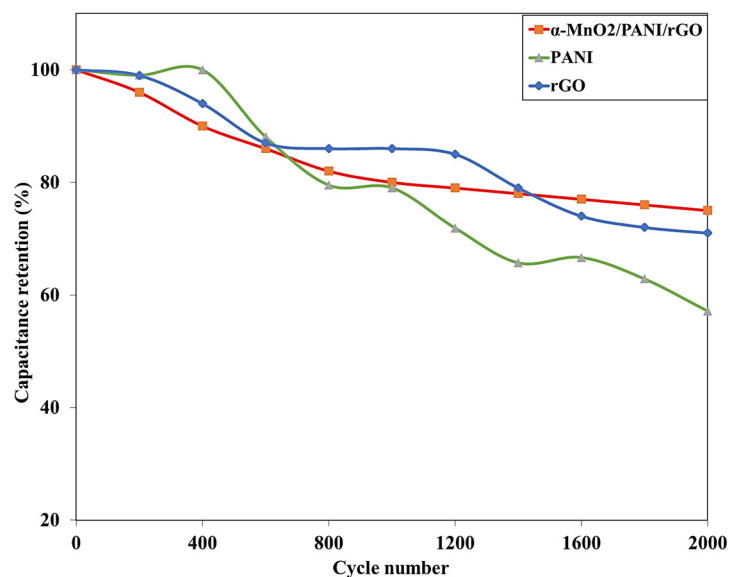


Figure 10. Cyclic stability of PANI, rGO and α -MnO₂/PANI/rGO nanocomposite.

4. Conclusions

As a conclusion of this work, we have successfully prepared an α -MnO₂/PANI/rGO nanocomposite and tested it for SC application. The novel approach of the in situ polymerization of PANI in optimized conditions in the presence of metal oxide yielded a good-quality composite material. The addition of a carbon-based material such as rGO into the α -MnO₂/PANI composite improved the specific capacitance of the material. The α -MnO₂/PANI/rGO electrode material showed better stability with 75% capacitance re-

tention after 2000 consecutive cycles. This work highlights the importance of rGO in the α -MnO₂/PANI composite for obtaining superior-quality composite materials. Furthermore, the in situ polymer coating on metal oxide greatly improved the film forming property of the material, which is one of the main requirements regarding the processability of the material toward device fabrication.

Author Contributions: V.V.K.: investigation, methodology, data curation and writing—original draft; P.H.P.: investigation, methodology, data curation and writing—original draft; T.D.D.: data curation and resources; S.A.J.: conceptualization, supervision, resources, writing—review and editing and project administration. All authors have read and agreed to the published version of the manuscript.

Funding: This research received no external funding.

Institutional Review Board Statement: Not applicable.

Informed Consent Statement: Not applicable.

Data Availability Statement: No data was used in this work.

Conflicts of Interest: The authors declare no conflict of interest.

References

1. Eedulakanti, S.R.; Gampala, A.K.; Rao, K.V.; Chakra, C.S.; Gedela, V.; Boddula, R. Ultrasonication Assisted Thermal Exfoliation of Graphene-Tin Oxide Nanocomposite Material for Supercapacitor. *Mater. Sci. Energy Technol.* **2019**, *2*, 372–376. [[CrossRef](#)]
2. Song, Z.; Zhang, G.; Deng, X.; Zou, K.; Xiao, X.; Momen, R.; Massoudi, A.; Deng, W.; Hu, J.; Hou, H.; et al. Ultra-Low-Dose Pre-Metallation Strategy Served for Commercial Metal-Ion Capacitors. *Nano-Micro Lett.* **2022**, *14*, 53. [[CrossRef](#)] [[PubMed](#)]
3. Weerasinghe, W.A.D.S.S.; Vidanapathirana, K.P.; Perera, K.S. Performance Evaluation of Polyaniline-Based Redox Capacitors with Respect to Polymerization Current Density. *AIMS Energy* **2018**, *6*, 593–606. [[CrossRef](#)]
4. Patil, V.S.; Thoravat, S.S.; Kundale, S.S.; Dongale, T.D.; Patil, P.S.; Jadhav, S.A. Synthesis and Testing of Polyaniline Grafted Functional Magnetite (Fe₃O₄) Nanoparticles and RGO Based Nanocomposites for Supercapacitor Application. *Chem. Phys. Lett.* **2023**, *814*, 140334. [[CrossRef](#)]
5. Khawas, K.; Kumari, P.; Daripa, S.; Oraon, R.; Kuila, B.K. Hierarchical Polyaniline-MnO₂-Reduced Graphene Oxide Ternary Nanostructures with Whiskers-Like Polyaniline for Supercapacitor Application. *ChemistrySelect* **2017**, *2*, 11783–11789. [[CrossRef](#)]
6. Lee, J.H.; Kim, H.-K.; Baek, E.; Pecht, M.; Lee, S.-H.; Lee, Y.-H. Improved Performance of Cylindrical Hybrid Supercapacitor Using Activated Carbon/Niobium Doped Hydrogen Titanate. *J. Power Sources* **2016**, *301*, 348–354. [[CrossRef](#)]
7. Lee, S.-H.; Kim, J.H.; Yoon, J.-R. Laser Scribed Graphene Cathode for Next Generation of High Performance Hybrid Supercapacitors. *Sci. Rep.* **2018**, *8*, 8179. [[CrossRef](#)] [[PubMed](#)]
8. Arslan, A.; Hür, E. Supercapacitor Applications of Polyaniline and Poly(N-Methylaniline) Coated Pencil Graphite Electrode. *Int. J. Electrochem. Sci.* **2012**, *7*, 12558–12572.
9. Beidaghi, M.; Gogotsi, Y. Capacitive Energy Storage in Micro-Scale Devices: Recent Advances in Design and Fabrication of Micro-Supercapacitors. *Energy Environ. Sci.* **2014**, *7*, 867. [[CrossRef](#)]
10. Liu, R.; Jiang, R.; Chu, Y.-H.; Yang, W.-D. Facile Fabrication of MnO₂/Graphene/Ni Foam Composites for High-Performance Supercapacitors. *Nanomaterials* **2021**, *11*, 2736. [[CrossRef](#)]
11. Patil, P.H.; Kulkarni, V.V.; Jadhav, S.A. An Overview of Recent Advancements in Conducting Polymer–Metal Oxide Nanocomposites for Supercapacitor Application. *J. Compos. Sci.* **2022**, *6*, 363. [[CrossRef](#)]
12. Wu, Q.; Xu, Y.; Yao, Z.; Liu, A.; Shi, G. Supercapacitors Based on Flexible Graphene/Polyaniline Nanofiber Composite Films. *ACS Nano* **2010**, *4*, 1963–1970. [[CrossRef](#)] [[PubMed](#)]
13. Ates, M.; Yildirim, M. The Synthesis of RGO/RuO₂, RGO/PANI, RuO₂/PANI and RGO/RuO₂/PANI Nanocomposites and Their Supercapacitors. *Polym. Bull.* **2020**, *77*, 2285–2307. [[CrossRef](#)]
14. Liu, W.; Wang, S.; Wu, Q.; Huan, L.; Zhang, X.; Yao, C.; Chen, M. Fabrication of Ternary Hierarchical Nanofibers MnO₂/PANI/CNT and Theirs Application in Electrochemical Supercapacitors. *Chem. Eng. Sci.* **2016**, *156*, 178–185. [[CrossRef](#)]
15. Hou, Y.; Cheng, Y.; Hobson, T.; Liu, J. Design and Synthesis of Hierarchical MnO₂ Nanospheres/Carbon Nanotubes/Conducting Polymer Ternary Composite for High Performance Electrochemical Electrodes. *Nano Lett.* **2010**, *10*, 2727–2733. [[CrossRef](#)] [[PubMed](#)]
16. Yu, G.; Hu, L.; Liu, N.; Wang, H.; Vosgueritchian, M.; Yang, Y.; Cui, Y.; Bao, Z. Enhancing the Supercapacitor Performance of Graphene/MnO₂ Nanostructured Electrodes by Conductive Wrapping. *Nano Lett.* **2011**, *11*, 4438–4442. [[CrossRef](#)]
17. Vignesh, V.; Velusamy, V.; Srinivasan, M.; Nirmala, R.; Ramasamy, P.; Panomsuwan, G.; Navamathavan, R. Thermo-Chemically Functionalized Porous Featured Bio-Carbon Based Asymmetric Supercapacitor for New Limits of Energy Storage. *Surf. Interfaces* **2022**, *35*, 102418. [[CrossRef](#)]

18. Vignesh, V.; Subramani, K.; Oh, M.-S.; Sathish, M.; Navamathavan, R. Synthesis of GNS-MnS Hybrid Nanocomposite for Enhanced Electrochemical Energy Storage Applications. *Mater. Chem. Phys.* **2019**, *230*, 249–257. [[CrossRef](#)]
19. He, Q.; Liu, J.; Liu, X.; Li, G.; Chen, D.; Deng, P.; Liang, J. A Promising Sensing Platform toward Dopamine Using MnO₂ Nanowires/Electro-Reduced Graphene Oxide Composites. *Electrochim. Acta* **2019**, *296*, 683–692. [[CrossRef](#)]
20. He, Q.; Liu, J.; Liu, X.; Li, G.; Deng, P.; Liang, J. Manganese Dioxide Nanorods/Electrochemically Reduced Graphene Oxide Nanocomposites Modified Electrodes for Cost-Effective and Ultrasensitive Detection of Amaranth. *Colloids Surf. B Biointerfaces* **2018**, *172*, 565–572. [[CrossRef](#)]
21. Amaechi, I.C.; Nwanya, A.C.; Ekwealor, A.B.C.; Asogwa, P.U.; Osuji, R.U.; Maaza, M.; Ezema, F.I. Electronic Thermal Conductivity, Thermoelectric Properties and Supercapacitive Behaviour of Conjugated Polymer Nanocomposite (Polyaniline-WO₃) Thin Film. *Eur. Phys. J. Appl. Phys.* **2015**, *69*, 30901. [[CrossRef](#)]
22. Kanta, U.; Thongpool, V.; Sangkhun, W.; Wongyao, N.; Wootthikanokkhan, J. Preparations, Characterizations, and a Comparative Study on Photovoltaic Performance of Two Different Types of Graphene/TiO₂ Nanocomposites Photoelectrodes. *J. Nanomater.* **2017**, *2017*, 2758294. [[CrossRef](#)]
23. Patil, K.T.; Nirmal, K.A.; Jadhav, S.A.; Patil, S.R.; Dongale, T.D.; Kim, D.; Patil, P.S. Bipolar Resistive Switching and Non-Volatile Memory Properties of MnO₂-Polyaniline (PANI) Nanocomposite. *Materialia* **2021**, *15*, 101026. [[CrossRef](#)]
24. Muthuchudarkodi, R.R.; Vedhi, C. Preparation and Electrochemical Characterization of Manganese Dioxide-Zirconia Nanorods. *Appl. Nanosci.* **2015**, *5*, 481–491. [[CrossRef](#)]
25. Lokhande, V.C.; Lokhande, A.C.; Lokhande, C.D.; Kim, J.H.; Ji, T. Supercapacitive Composite Metal Oxide Electrodes Formed with Carbon, Metal Oxides and Conducting Polymers. *J. Alloys Compd.* **2016**, *682*, 381–403. [[CrossRef](#)]
26. Mezgebe, M.M.; Xu, K.; Wei, G.; Guang, S.; Xu, H. Polyaniline Wrapped Manganese Dioxide Nanorods: Facile Synthesis and as an Electrode Material for Supercapacitors with Remarkable Electrochemical Properties. *J. Alloys Compd.* **2019**, *794*, 634–644. [[CrossRef](#)]
27. Jadhav, S.A.; Dhas, S.D.; Patil, K.T.; Moholkar, A.V.; Patil, P.S. Polyaniline (PANI)-Manganese Dioxide (MnO₂) Nanocomposites as Efficient Electrode Materials for Supercapacitors. *Chem. Phys. Lett.* **2021**, *778*, 138764. [[CrossRef](#)]
28. Durai, S.C.V.; Prasad, L.G.; Kumar, E.; Muthuraj, D.; Jothy, V.B. Preparation and investigation on electric impedance modules and dielectric properties of polyaniline/Manganese dioxide nanocomposites. *Int. J. Creat. Res. Thoughts* **2018**, *6*, 543–547.
29. Li, H.; He, Y.; Pavlinek, V.; Cheng, Q.; Saha, P.; Li, C. MnO₂ Nanoflake/Polyaniline Nanorod Hybrid Nanostructures on Graphene Paper for High-Performance Flexible Supercapacitor Electrodes. *J. Mater. Chem. A* **2015**, *3*, 17165–17171. [[CrossRef](#)]
30. Yavuz, S.; Bandaru, P.R. Ag Nanowire Coated Reduced Graphene Oxide/n-Silicon Schottky Junction Based Solar Cell. In Proceedings of the 2016 IEEE Conference on Technologies for Sustainability (SusTech), Phoenix, AZ, USA, 9–11 October 2016; 2016; pp. 265–269.
31. Dhawale, D.S.; Vinu, A.; Lokhande, C.D. Stable Nanostructured Polyaniline Electrode for Supercapacitor Application. *Electrochim. Acta* **2011**, *56*, 9482–9487. [[CrossRef](#)]
32. Hsieh, M.-C.; Chen, B.-H.; Hong, Z.-Y.; Liu, J.-K.; Huang, P.-C.; Huang, C.-M. Fabrication of 5 V High-Performance Solid-State Asymmetric Supercapacitor Device Based on MnO₂/Graphene/Ni Electrodes. *Catalysts* **2022**, *12*, 572. [[CrossRef](#)]
33. Yu, J.; Fu, N.; Zhao, J.; Liu, R.; Li, F.; Du, Y.; Yang, Z. High Specific Capacitance Electrode Material for Supercapacitors Based on Resin-Derived Nitrogen-Doped Porous Carbons. *ACS Omega* **2019**, *4*, 15904–15911. [[CrossRef](#)] [[PubMed](#)]
34. Han, J.; Li, L.; Fang, P.; Guo, R. Ultrathin MnO₂ Nanorods on Conducting Polymer Nanofibers as a New Class of Hierarchical Nanostructures for High-Performance Supercapacitors. *J. Phys. Chem. C* **2012**, *116*, 15900–15907. [[CrossRef](#)]
35. Li, J.; Xie, H.; Li, Y.; Liu, J.; Li, Z. Electrochemical Properties of Graphene Nanosheets/Polyaniline Nanofibers Composites as Electrode for Supercapacitors. *J. Power Sources* **2011**, *196*, 10775–10781. [[CrossRef](#)]
36. Teli, A.M.; Beknalkar, S.A.; Pawar, S.A.; Dubal, D.P.; Dongale, T.D.; Patil, D.S.; Patil, P.S.; Shin, J.C. Effect of Concentration on the Charge Storage Kinetics of Nanostructured MnO₂ Thin-Film Supercapacitors Synthesized by the Hydrothermal Method. *Energies* **2020**, *13*, 6124. [[CrossRef](#)]

Disclaimer/Publisher's Note: The statements, opinions and data contained in all publications are solely those of the individual author(s) and contributor(s) and not of MDPI and/or the editor(s). MDPI and/or the editor(s) disclaim responsibility for any injury to people or property resulting from any ideas, methods, instructions or products referred to in the content.